PCCP

ROYAL SOCIETY OF CHEMISTRY

PAPER

View Article Online
View Journal | View Issue

Cite this: *Phys. Chem. Chem. Phys.*, 2024, **26**, 26314

Influence of H-bonding on the crystalline structures and ferroelectric and piezoelectric properties of novel nanogenerators of the lithium salt of 6-amino hexanoic acid incorporated poly(vinylidene fluoride) composites†

Ananya Aishwarya, Akanksha Adaval, Suvankar Mondal, Titas Dasgupta and Arup R. Bhattacharyya *

Received 22nd June 2024,
Accepted 25th September 2024

DOI: 10.1039/d4cp02497d

rsc.li/pccp

The lithium salt of 6-amino hexanoic acid (Li–AHA) was melt-mixed with poly(vinylidene fluoride) (PVDF), wherein the Li–AHA concentration was varied between 1–15 wt% with the aim of establishing hydrogen bonding between the NH_2 functionality of Li–AHA and the $-CF_2$ moieties of PVDF. This was followed by compression-moulding as well as solution-casting to make PVDF/Li–AHA composite thin films. FTIR analysis established interactions between the $-CF_2$ groups in PVDF with amine functional moieties of Li–AHA. Moreover, FTIR analysis estimated that the solution-cast PVDF/Li–AHA composite of 15 wt% Li–AHA exhibited the highest polar phase fraction of ~60%. Furthermore, ferroelectric analysis showed that the solution-cast PVDF/Li–AHA composite of 15 wt% Li–AHA exhibited the highest remnant polarization of 0.07 μC cm^{-2} (at 50 Hz, 1000 V) from the polarization *versus* electric field loop. Finally, energy harvester devices were fabricated using compression-moulded and solution-cast PVDF/Li–AHA composite films, in which a maximum output voltage of ~110 V was obtained in the solution-cast PVDF/Li–AHA composite of 15 wt% Li–AHA. The devices also displayed a maximum power density of 75 μW cm^{-2} and 85 μW cm^{-2} for those fabricated *via* compression-moulding and solution-casting, respectively. Three different capacitors were efficiently charged by the tapping of the devices made from solution-cast and compression-moulded composite films of 15 wt% Li–AHA. An interrelationship between processing, structure and properties was successfully established in the PVDF/Li–AHA composites with greatly enhanced piezoelectric properties.

1. Introduction

The advancements in the field of electronics emphasize the development of portable and adaptable gadgets for applications related to health and wellness monitoring, sensor networks, synthetic muscles, transducers, microbalances, vibration sensors, and engineered tissue structures.[1–5] Piezoelectric polymers hold significant promise for such applications, as they can harness deformations triggered by external forces such as pressure, mechanical vibration, stretching/compression, bending, or twisting.[6] Poly(vinylidene fluoride) (PVDF) has attracted focus in these areas, due to its piezoelectric nature, with numerous benefits such as biocompatibility, chemical resistance, excellent film-forming ability, affordability, high strength, flexibility, ease of processing, high piezoelectric coefficients *etc.*[7,8] PVDF exhibits predominantly three crystalline phases: α, β and γ with different chain conformations, of which the α-phase is thermodynamically the most stable.[7] Considering the chain structure of PVDF, due to the overall cancellation of the oppositely placed fluorine atoms in the α-phase, it shows net zero dipole moment.[9,10] Interestingly, due to the unidirectional orientation of the dipole chains, the β and γ-phases of PVDF are polar phases.[11,12] Further, β and γ-phases exhibit a net non-zero dipole moment in PVDF.[13,14] Out of all the forms of PVDF, the β-phase exhibits higher piezoelectric properties due to the dipolar arrangement of the chains and the highest dipole moment (2.1 Debye).[15] In the context of PVDF, which has repeating units of $-CH_2-CF_2-$, the β-phase conformation arranges these dipoles in a way that maximizes the net dipole moment along

Department of Metallurgical Engineering and Materials Science, Indian Institute of Technology Bombay, Powai, Mumbai 400076, India. E-mail: arupranjan@iitb.ac.in; Fax: +91 22 2572 6975; Tel: +91 22 2576 7634

† Electronic supplementary information (ESI) available: Characterization and measurements; polarised optical microscopic images; a table depicting the variation of roughness parameters; FTIR spectra, XRD analysis; PE-loops, components and working of piezoelectric device, variation of power density with load resistance, and 5 LEDs lit by the power generated from the solution-cast PVDF/Li–AHA composite with 15 wt% Li–AHA (Video SV). See DOI: **https://doi.org/10.1039/d4cp02497d**

the polymer chain. The value of 2.1 Debye represents the dipole moment of a single monomer unit in the β-phase, which contributes to the overall piezoelectric properties of the material. Due to this advantage, PVDF is widely used in various industrial applications due to its higher dielectric constant and enhanced electroactive response, in comparison to other polymers.[16,17]

The electroactive properties of PVDF have been exploited in various applications owing to its ferroelectric and piezoelectric behaviour.[18,19] Thus, the improvement of the electroactive phases of PVDF through various techniques has been extensively investigated.[20,21] The amount and alignment of PVDF polymorphs are influenced by different processing techniques like stretching, poling, rolling, solvent casting, electrospinning, *etc.*[22–28] One such method involves the introduction of micro/nanomaterials or modifiers in PVDF to obtain polar phases of PVDF and to understand the phase transformation and its enhancement influenced by the addition of micro/nanomaterials, organic modifiers, and salts.[28–32] Vijayakumar *et al.* studied the influence of benzyl triphenyl phosphonium chloride and tetrabutyl ammonium perchlorate on the crystallization of PVDF from its molten state and reported that the inclusion of these salts led to enhancement of the polar phases within the PVDF structure.[29] Xing *et al.* incorporated 1-butyl-3-methylimidazolium hexafluorophosphate as filler with PVDF and observed that a maximum of ~80% γ-crystalline form was formed at 2 wt% of the filler in PVDF.[30] Jana *et al.* fabricated piezoelectric energy harvesters by incorporating a hydrated metal salt ($MgCl_2 \cdot 6H_2O$) (Mg-salt) into PVDF, in which they reported a polar fraction of ~90% at 2.25 wt% of the hydrated metal salt, and the fabricated device showed an output voltage of 4 V at 2 wt% of the hydrated metal salt.[31] Dias *et al.* made composite films of PVDF and its copolymers with ionic liquid (1-ethyl-3-methylimidazolium bis(trifluoromethanesulfonyl) imide) *via* solvent casting, wherein they reported that the ionic liquid in PVDF induced β-phase formation in PVDF and in its copolymers.[32] Li *et al.* fabricated ZnO modified with (*n*-propylamine) and a silane coupling agent, which was incorporated into PVDF and reported a d_{33} value ~34.7 pC N^{-1} of the composite film, while neat PVDF–TrFE film exhibited a d_{33} value ~20 pC N^{-1}.[33]

In the current work, a novel Li-salt of 6-amino hexanoic acid (Li–AHA) was incorporated to prepare PVDF/Li–AHA composites, wherein the amine group of Li–AHA salt is expected to establish hydrogen bonding (H-bonding) with the fluorine moiety of PVDF, thereby inducing polar crystalline phase of PVDF. Further, a greater extent of interfacial interaction is expected to be obtained with increasing the Li–AHA concentration in the PVDF/Li–AHA composites, which may result in an enhanced degree of polar fraction in the respective PVDF composite. Moreover, melt-mixed PVDF/Li–AHA composites were further processed *via* two different routes namely, compression-moulding and solution-casting, to investigate the effect of the processing method on polar phase fraction and piezoelectric properties of corresponding PVDF/Li–AHA composites. The variation of spherulitic superstructures in the composite film has been investigated through polarizing optical microscopy, while the structural investigations and the subsequent formation of polar phases have been observed *via* X-ray diffraction and FTIR spectroscopy. Furthermore, ferroelectric and piezoelectric properties have also been explored and compared in compression-moulded and solution-cast PVDF/Li–AHA composite films. Furthermore, nanogenerator devices have been fabricated using compression-moulded and solution-cast composite films to demonstrate piezoelectric energy harvesting applications. A thorough investigation has been conducted to establish the relationship between the processing method employed, the resulting structure, and the properties of PVDF/Li–AHA composites.

2. Experimental section

2.1. Materials

Poly(vinylidene flouride) (PVDF) (Kynar 720, density = 1.78 g cm^{-3}, T_m = 168 °C) was procured from Arkema, India. Dimethylformamide (DMF) was obtained from Sigma Aldrich, India. The Li-salt of 6-amino hexanoic acid (Li–AHA) was obtained by neutralization of 6-aminohexanoic acid (AHA; Sigma-Aldrich, USA) with lithium hydroxide in deionized water to obtain the lithium salt of 6-aminohexanoic acid (Li–AHA).[32] To synthesize the lithium salt of 6-aminohexanoic acid (Li–AHA), 6-aminohexanoic acid (AHA), a compound that contains both an amino group ($-NH_2$) and a carboxylic acid group (–COOH), was neutralized using lithium hydroxide (LiOH). This reaction occurs in deionized water as the solvent.

In the neutralization process, the carboxylic acid group (–COOH) of AHA reacts with the lithium hydroxide base. The hydroxide ion (OH^-) from lithium hydroxide deprotonates the carboxyl group (–COOH), converting it to a carboxylate anion ($-COO^-$). Simultaneously, the lithium ion (Li^+) associates with the deprotonated carboxyl group, forming the lithium salt of 6-aminohexanoic acid (Li–AHA) and water as a by-product. The water was completely evaporated and salt crystals were obtained, which were used in further processes.

2.2. Preparation of PVDF/Li–AHA composites

PVDF/Li–AHA composites with varying concentrations of Li–AHA salt (1–15 wt%) were prepared *via* melt-mixing in a conical twin screw micro-compounder (5 cc micro-compounder, Xplore-5, Netherlands) for 10 minutes, at 240 °C. The extrudate was then collected, cooled to room temperature, and cut into small pieces for further processing. Two different processing methods *viz.* (i) compression-moulding and (ii) solution-casting were adopted to prepare the PVDF/Li–AHA composite films. The compression-moulded film (with an average thickness of ~50 μm) was obtained at ~240 °C and ~20 MPa using cut extrudates in a hot press. For solution-casting, initially the extrudates were dissolved in DMF at ~60 °C, until no residue of the extrudate remained undissolved. The composite dispersion was then drop-cast onto a Petri-dish and vacuum dried at ~100 °C until the solvent completely evaporated and a solution-cast film of average thickness of ~40 μm was obtained.

2.3. Characterization

2.3.1. Polarized optical microscopy. A polarized optical microscope (Leica 2700LP, Leica, Germany) was utilized to

observe the crystalline superstructure in pure PVDF and PVDF/Li–AHA composite films. Compression-moulded and solution-cast pure PVDF and PVDF/Li–AHA composite films (thickness ~40 μm) were melt-pressed on a glass slide for observation under an optical microscope.

2.3.2. Scanning probe microscopy. Scanning probe microscopy (Bruker, Multimode Nanoscope-IV) was used to characterize surface roughness and topography at a nanoscale level. Compression-moulded and solution-cast pure PVDF and PVDF/Li–AHA composite films (5 mm × 5 mm) of thickness ~40 μm were used for scanning probe microscopy.

2.3.3. Fourier transform infrared (FTIR) spectroscopy. FTIR analysis (Bruker 3000 Hyperion microscope, Vertex 80) of the compression-moulded and solution-cast pure PVDF film and PVDF/Li–AHA composite thin films (~40 μm) was carried out in the range 400–4000 cm^{-1} at 0.2 cm^{-1} resolution.

2.3.4. Wide angle X-ray diffraction (WAXD). WAXD measurements were carried out using an X-ray diffractometer (X'Pert Pro, PANalytical) with 1.54 Å incident line of Cu-K_α radiation in the range of 2θ = 10–45°.

2.3.5. Ferroelectric analysis. Ferroelectric polarization investigations for both pure PVDF and PVDF/Li–AHA composite films (thickness ~40 μm) were conducted (TF Analyzer 2000, Aixact, Germany). Triangular waveforms at frequencies of 1 Hz and 50 Hz were applied with variable voltages.

2.3.6. Piezo force microscopy (PFM). Piezoelectric properties of pure PVDF and PVDF/Li–AHA composite films (5 mm × 5 mm) were measured in the contact mode with a scanning probe microscope (Agilent 5500). During measurements, a silicon conductive probe coated with Cr/Pt was used (force constant = 3 N m^{-1}). Subsequently, the tip was biased with AC voltage of 10 V (AC voltage) and the DC voltage was varied from −10 V to +10 V. The cantilever tip had a deflection sensitivity of 109 nm V^{-1} and x128 gains. The piezoelectric coefficient (d_{33}) of the pure PVDF and PVDF/Li–AHA composite films was calculated using eqn (1):

$$d_{33} = \frac{\text{Amplitude (V)} \times \text{Deflection sensitivity}\left(\frac{\text{nm}}{\text{V}}\right)}{\text{AC Bias (V)} \times \text{Gain}} \quad (1)$$

2.3.7. Piezoelectric device testing. Pure PVDF and PVDF/Li–AHA composite films, produced *via* solution-casting and compression-moulding, were used to fabricate into piezoelectric devices. These films, with dimensions of 3 × 1.5 cm^2 and thickness of ~50 μm, were sandwiched between copper foils, which served as electrodes. The entire device (the film sandwiched between copper electrodes) was completely laminated, which ensured full adherence of the electrodes (copper foils) to the sample surface (PVDF composite). The copper foils used as electrodes adhered well to the sample surface to ensure consistent electrical contact across the entire area. Even after lamination, the rigidity of the copper foils was sufficient to maintain their shape and ensure a stable connection with the sample. However, they were also flexible enough to conform to the surface of the PVDF sample, allowing for uniform contact. For our studies, the copper foils used in the device fabrication were of ~160 μm thickness. These copper foil electrodes were connected to a digital oscilloscope (Tektronix TBS 1072B), using thin copper wires. To ensure stable contact between the composite film and electrodes, the assembly was wrapped with Kapton tape, providing insulation. The piezoelectric voltage was generated by finger tapping on the device, and its response was observed with an oscilloscope.

3. Results and discussions

3.1. Morphological observations *via* polarized optical microscopy (POM)

Polarized optical microscopic observations (Fig. 1) reveal the surface morphology of compression-moulded and solution-cast pure PVDF (Fig. 1(a) and (c)) and PVDF/Li–AHA composite of 15 wt% Li–AHA concentration (Fig. 1(b) and (d)). In addition, Fig. S1(a)–(h) (ESI†) shows the representative POM images of compression-moulded, solution-cast and PVDF/Li–AHA composite films with varying Li–AHA concentration. The average size of PVDF spherulites was measured using ImageJ software which allows for the precise measurement of spherulite diameters by analyzing optical micrographs of the PVDF composite films. The images were first captured at a suitable magnification and then the spherulite boundaries were manually traced within the software. The average spherulite size was calculated by measuring multiple spherulites across different regions of the sample to ensure a representative average value. This method provides an accurate estimation of the spherulite size distribution in the films.

In general, PVDF crystallizes predominantly in the α-crystalline form. The average spherulite size of solution-cast pure PVDF (~33.5 μm) is smaller as compared to the compression-moulded pure PVDF (~46.7 μm) film. The faster rate of crystallization of PVDF in the case of solution-casting as compared to compression-moulding has been observed

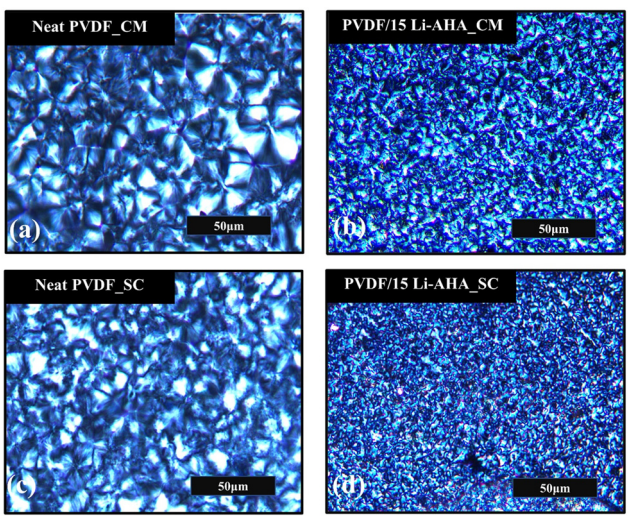

Fig. 1 Polarised optical microscopic images of (a) and (b) compression-moulded and (c) and (d) solution-cast films of (a) and (c) neat PVDF and (b) and (d) PVDF/Li–AHA composite of 15 wt% Li–AHA.

previously.[34,35] Lower drying temperatures in the case of solution-casting result in a higher rate of nucleation, which lead to smaller size of spherulites.[34] However, in the case of compression-moulding, the crystallization process is suddenly arrested, which inhibits the rate of crystallization. Also, with the decrease in the isothermal crystallization temperature during solution-casting, the crystallization rate increases, which is less in the case of compression-moulding due to the faster cooling that otherwise slows down the rate of crystallization, leading to formation of bigger spherulites.[35] In this context, we have carried out a comparative study for both the systems *via* polarized optical spectroscopy regarding the average spherulite size in the PVDF/Li–AHA composites. The incorporation of Li–AHA facilitates the formation of smaller average spherulitic structures in the PVDF/Li–AHA composite prepared *via* compression-moulding and solution-casting as compared to neat PVDF. The average spherulite size decreases progressively from $\sim$46.7 $\pm$ 1.5 μm for pure PVDF to 23.46 $\pm$ 1.51, 10.34 $\pm$ 1.34, and 8.35 $\pm$ 1.09 μm in the PVDF/Li–AHA composite of 4, 10 and 15 wt% Li–AHA concentration, respectively, in the case of the compression-moulded composite films (Fig. S1(i), ESI†). Furthermore, the average spherulite size decreases progressively from $\sim$33 $\pm$ 1.1 μm for pure PVDF to 18.16 $\pm$ 0.81, 5.39 $\pm$ 0.76, and 3.24 $\pm$ 0.65 μm in PVDF/Li–AHA composite of 4, 10 and 15 wt% Li–AHA concentration, respectively, in the case of the solution-cast composite films (Fig. S1(i), ESI†). Fig. S1(i) (ESI†) shows the gradual decrease in the average spherulite size of PVDF on incorporation of 1–15 wt% of Li–AHA in PVDF/Li–AHA composites. So, it is evident that the average spherulite size in the solution-cast PVDF/Li–AHA composite is lower than the corresponding composite of the compression-moulded film. These observations signify that Li–AHA acts as a heterogenous nucleating centre during PVDF crystallization, which creates a large number of nucleating sites with the concomitant growth of smaller average spherulite size.

Fig. 2 exhibits the progression of surface roughness of pure PVDF and PVDF/Li–AHA composite films of 6 and 15 wt% of Li–AHA concentration made *via* compression-moulding and solution-casting as observed using scanning probe microscopy (SPM). As reported in Table S1 (ESI†), the RMS roughness value (S_q) increases from $\sim$4.3 to $\sim$11.6 nm when transitioning from pure PVDF to the PVDF/Li–AHA composite with 15 wt% Li–AHA concentration for the compression-moulded films. Conversely, for the solution-cast films, the RMS roughness value rises from

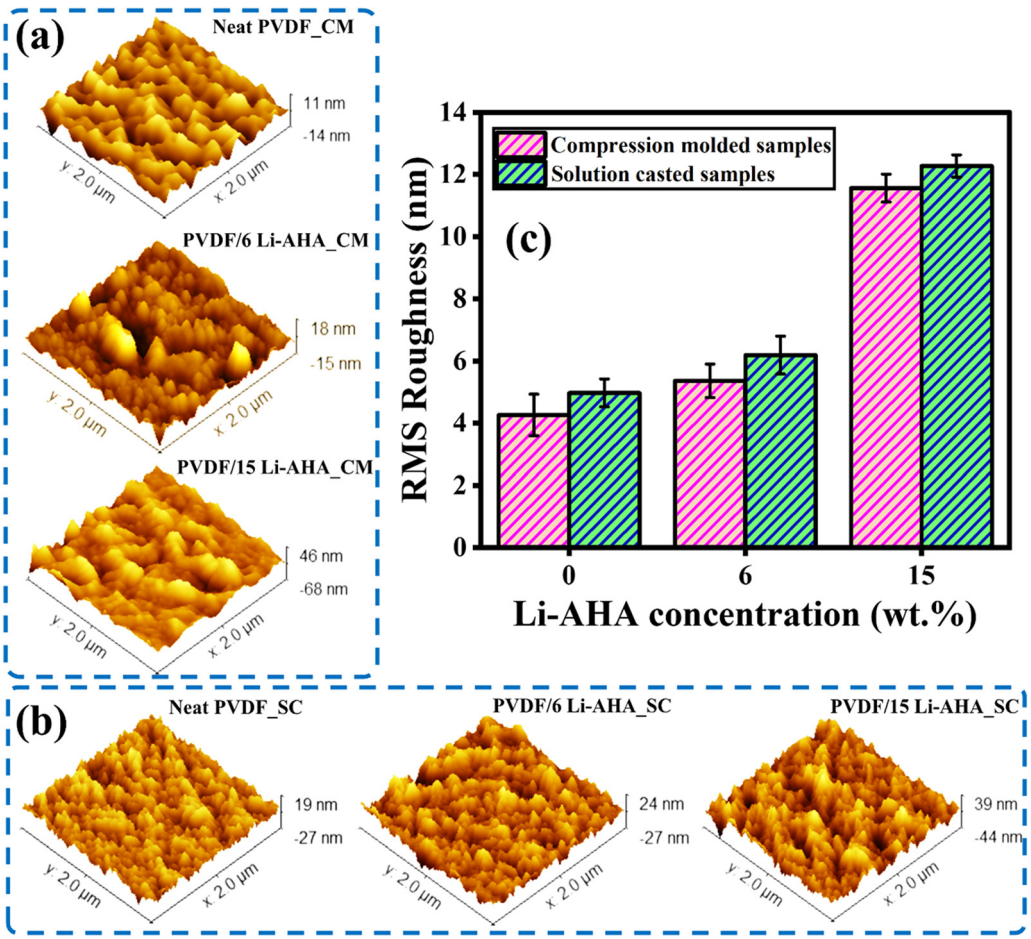

Fig. 2 AFM images showing the surface roughness of (a) compression-moulded films, (b) solution-cast films and (c) progression of surface roughness with varying Li–AHA concentration for compression-moulded and solution-cast pure PVDF and PVDF/Li–AHA composite films.

~4.9 nm to ~12.3 nm with the same concentration of Li–AHA. Moreover, the maximum height of the roughness value increases from ~10.9 nm for pure PVDF to ~45.7 nm for PVDF/Li–AHA composite films containing 15 wt% Li–AHA for the compression-moulded films. Similarly, for solution-cast films, the height of the roughness value increases from ~18.8 nm for pure PVDF to ~38.7 nm for the composite with 15 wt% Li–AHA. This increase in height is comparable to the increase in depth, as shown in Table S1 (ESI†), indicating the combined contribution of both elevations and depressions within the roughness. The addition of Li–AHA molecules increases roughness of the composite films caused by the random overlapping on the PVDF backbone.[36] The formation of these heights and pits stems from the differences in atomic stacking direction between the PVDF chains and Li–AHA molecules. The physical bond relies on the interaction among the adjacent elevations, which serve as hooks to promote bonding and aid in the continued crystallization of PVDF.[37] Further, AFM topographical images also illustrate the surface roughness of PVDF in the PVDF/Li–AHA composites, where the preferential orientation of the crystalline grains increases with the increase of the Li–AHA concentration in the respective composite.

3.2. Interfacial interaction studies *via* Fourier transform infrared (FTIR) spectroscopy

FTIR spectroscopy was carried out to explore the interaction between Li–AHA and PVDF chains. The corresponding FTIR spectra of pure PVDF and PVDF/Li–AHA composite films prepared *via* solution-casting (Fig. 3(a)) and compression-moulding (Fig. 3(b)) are presented from ~850–1300 cm^{11}. Additionally, Fig. S2(a)–(d) (ESI†) displays FTIR spectra of compression-moulded and solution-cast PVDF/Li–AHA composites of all the compositions. Prominent peaks detected at ~875 and ~1180 cm^{-1} denote $-CF_2$ stretching vibrations in PVDF.[38] A prominent peak shift in the ν_s (CF_2) stretching band at ~875 cm^{-1} is observed in case of compression-moulded as well as solution-cast PVDF/Li–AHA composite films. The ν_s (CF_2) band obtained at ~875 cm^{-1} for the neat PVDF film shifts progressively to higher wavenumbers (~881 and 883 cm^{-1}) in the PVDF/Li–AHA composite with increased Li–AHA concentration (Fig. 3(c)). The maximum peak shift is

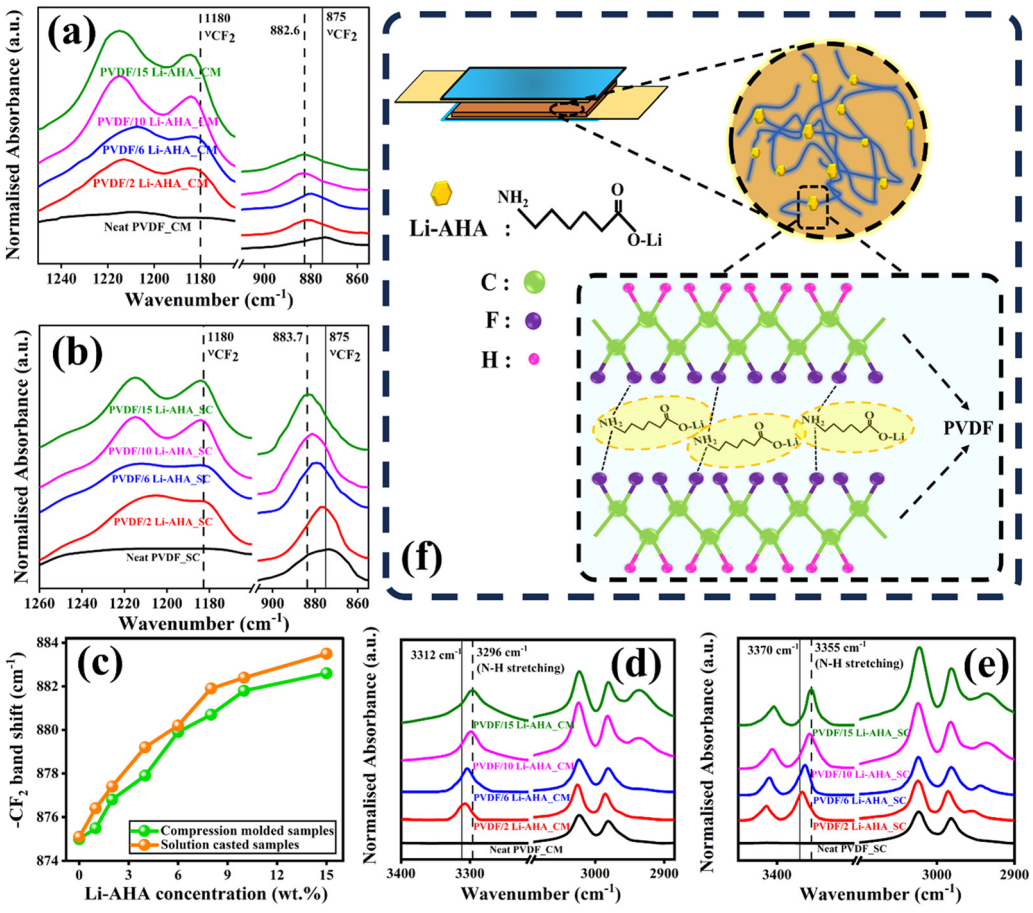

Fig. 3 FTIR spectra indicating the $-CF_2$ peak shift in (a) compression-moulded, (b) solution-cast pure PVDF and PVDF/Li–AHA composite films, (c) shift in the $-CF_2$ peak with the increase in Li–AHA concentration for compression-moulded and solution-cast films, FTIR spectra indicating the $-NH_2$ peak shift in (d) compression-moulded and (e) solution-cast pure PVDF and PVDF/Li–AHA composite films, and (f) a schematic representation of the mechanism of interaction between PVDF chains and Li–AHA.

observed in the PVDF/Li–AHA composite film with 15 wt% Li–AHA in the compression-moulded and solution-cast films. Further, the band at ~1180 cm^{-1} corresponding to ν_s (CF_2), depicts a prominent peak shift in the compression-moulded PVDF/Li–AHA composite films, which suggests a greater extent of interfacial interaction.[38] However, this could not be manifested in the case of the solution-cast PVDF/Li–AHA composite films, due to which no peak shift in ~1180 cm^{-1} could be observed. Moreover, the absorbance peak at ~3290–3350 cm^{-1} is present due to the –NH stretching vibration associated with $-NH_2$ functional group in Li–AHA as exhibited in Fig. S2(e) (ESI†).[39] Pure PVDF films did not show an absorbance peak at ~3295 cm^{-1} but it gradually appeared at ~3312 cm^{-1} in the case of compression-moulded PVDF/Li–AHA composite and at ~3370 cm^{-1} in the case of compression-moulded PVDF/Li–AHA composite as Li–AHA is incorporated into PVDF, as depicted in Fig. 3(d) and (e). Further, in the case of the compression-moulded PVDF/Li–AHA composite, the –NH peak shifts from ~3312 cm^{-1} in the PVDF/Li–AHA composite of 1 wt% Li–AHA to ~3296 cm^{-1} in the PVDF/Li–AHA composite of 15 wt% Li–AHA (Fig. 3(d)). In the case of the solution-cast PVDF/Li–AHA composite, the –NH peak shifts from ~3370 cm^{-1} in the PVDF/Li–AHA composite of 1 wt% Li–AHA to ~3355 cm^{-1} in the PVDF/Li–AHA composite of 15 wt% Li–AHA (Fig. 3(e)). This progressive shift of the ν_s (CF_2) band and corresponding shift in the –NH absorbance peak of Li–AHA indicate the increased H-bonding between the $-NH_2$ functional moiety of Li–AHA and the $-CF_2$ groups of PVDF with increased Li–AHA concentration in PVDF/Li–AHA composite. In light of the above, we propose a schematic representation of H-bonding between the $-CF_2$ groups of PVDF and $-NH_2$ moiety of Li–AHA in the PVDF/Li–AHA composite (Fig. 3(f)).[40,41]

Furthermore, the dipole moment of the filler material plays a crucial role in aligning the dipoles within the PVDF matrix. A filler with a strong dipole can enhance the polar β-phase nucleation by interacting with the polar segments of the PVDF chains. This interaction favors the formation of the β-phase, which has a higher dipole alignment compared to the non-polar α-phase. As the dipoles of the PVDF and the filler interact, this can help stabilize the β-phase structure, particularly under poling or mechanical stretching.[42] By increasing the separation between PVDF chains, the filler can reduce the van der Waals forces that normally hold the chains together in the non-polar α-phase. This reduction in intermolecular forces enhances the rotational freedom of the PVDF dipoles, making it easier for them to reorient from the non-polar α-phase to the polar β-phase during stretching or poling. Additionally, by reducing the van der Waals forces, the filler can decrease the energy barrier for the phase transition, thereby facilitating the formation of the β-phase.[43]

3.3. Development of electroactive (β/γ) phases

The FTIR spectra (Fig. 4(a) and (b)) provide an idea of the various phases that are present in the compression-moulded and solution-cast pure PVDF and PVDF/Li–AHA composite films, respectively. The absorption bands at ~487 cm^{-1} (CF_2 wagging and bending), ~532 cm^{-1} ($-CF_2$ bending), ~615, ~765 cm^{-1} ($-CF_2$ bending), ~875 cm^{-1} ($-CF_2$ stretching) and ~975 cm^{-1} (C–H out of plane deformations) indicate the presence of α-phase of PVDF.[44] Further, the stretching band at ~840 cm^{-1} ($-CH_2$ rocking and $-CF_2$ asymmetric stretching) suggests the existence of both polar phases (β and γ-crystalline phases). Absorption bands at ~1234 cm^{-1} and 1275 cm^{-1} (C–F out-of-plane deformations) are specifically associated with the γ-phase and β-phase of PVDF, respectively.[45] It is also noteworthy that absorption peaks representative of the polar phase/s at 840 cm^{-1} and shoulders at ~1234 cm^{-1} and ~1275 cm^{-1} become more prominent, which correspond to a higher intensity of the normalized absorption peaks with the progressive increase of Li–AHA in the PVDF/Li–AHA composite. The PVDF/Li–AHA composite of 15 wt% Li–AHA exhibits the highest intensities of the normalized absorption bands of the electroactive phase than the composite of other Li–AHA concentration, representing the presence of the highest electroactive phase fraction. FTIR plots of compression-moulded and solution-cast neat PVDF and the remaining compositions of PVDF/Li–AHA composites are depicted in Fig. S2 (ESI†).

Further, WAXD analysis was carried out to corroborate the observations from FTIR analysis in compression-moulded and solution-cast pure PVDF and PVDF/Li–AHA composite films (Fig. 4). WAXD patterns of neat PVDF and the remaining compositions of the PVDF/Li–AHA composite films are depicted in Fig. S3 (ESI†). Fig. 4(c) and (d) show two prominent peaks at 2θ = 18.4°and 19.9°, corresponding to the α-crystalline phase (monoclinic crystal structure) of [020] and [110/200] diffraction planes, respectively. A weak diffraction peak is detected at 2θ = 17.7° corresponding to the non-polar α-crystalline phase at a diffraction plane of [100].[46] Further, the existence of the electroactive (β/γ) phase is established from the peak at 20.1° [110]. The diffraction peak at 19.9° shifts towards higher 2θ values indicating that the α-phase gets converted to the β (orthorhombic)/γ-crystalline phase (monoclinic) in the PVDF/Li–AHA composite with the incorporation of Li–AHA. The PVDF/Li–AHA composite of 15 wt% Li–AHA shows a peak at 2θ = ~20.1°, which indicates the existence of polar phases.[39] Dipolar interactions and H-bonding at the interface among PVDF chains, Li–AHA, and DMF may promote a more organized packing of CH_2–CF_2 dipoles, thus facilitating development of the *trans* (TTT) conformation, which represents the electroactive phases.[46] Consequently, a higher polar phase fraction is observed in the PVDF/Li–AHA composite films prepared *via* solution-casting compared to those produced through compression-moulding.

The polar phase fraction of PVDF was calculated using eqn (2), which is depicted in Fig. 4(e) with varying concentration of Li–AHA in the PVDF/Li–AHA composites:

$$F(p) = \frac{A_p}{\left(\frac{K_p}{K_\alpha}\right) \times A_\alpha + A_p} \quad (2)$$

where, A_p and A_α refer to absorption intensities and K_p (7.7 ×

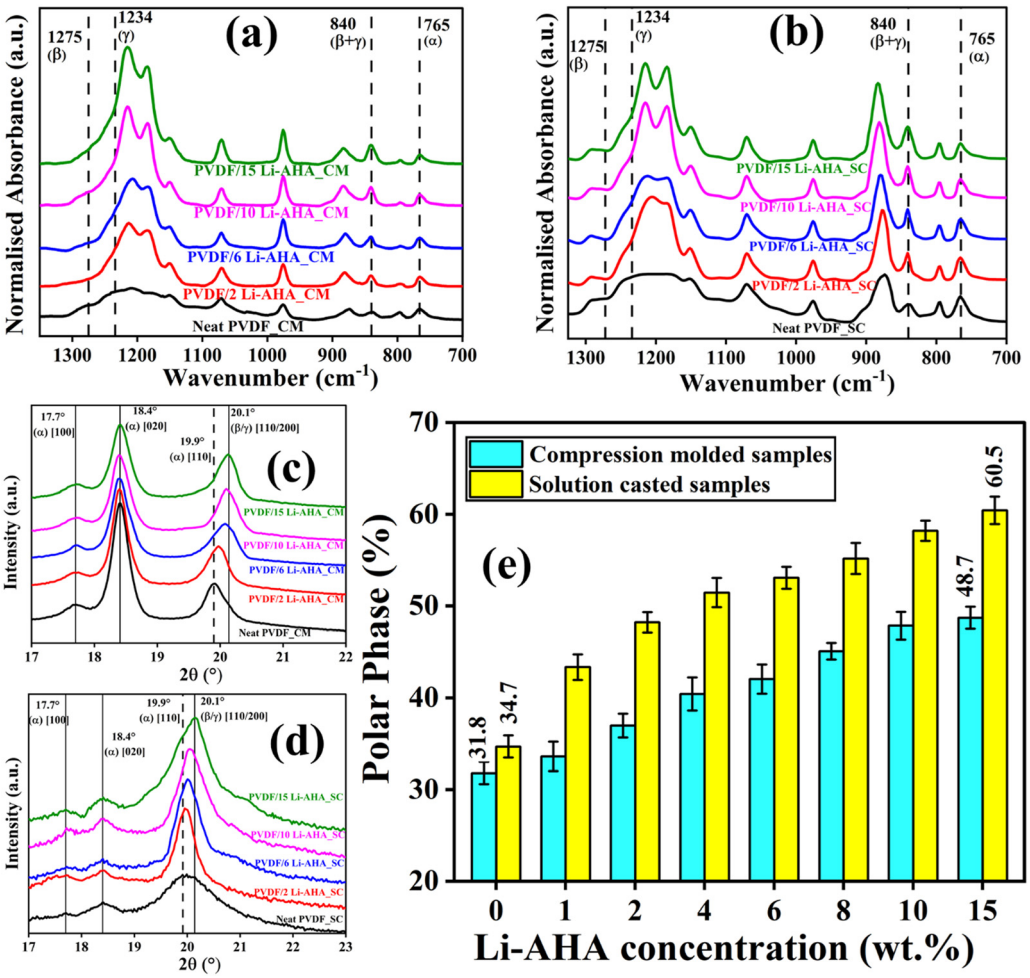

Fig. 4 Representative FTIR spectra of (a) compression-moulded and (b) solution-cast neat PVDF and PVDF/Li–AHA composites, representative WAXD patterns of (c) compression-moulded and (d) solution-cast neat PVDF and PVDF/Li–AHA composites, (e) variation of the polar phase content (%) with the increase in Li–AHA concentration in compression-moulded and solution-cast neat PVDF and PVDF/Li–AHA composites.

10^4 cm^2 mol^{-1}) and K_α (6.1×10^4 cm^2 mol^{-1}) refer to absorption coefficients at 840 and 765 cm^{-1}, respectively.[38]

Fig. 4(e) depicts the variation of the polar phase content (β/γ-phase) with Li–AHA concentration for compression-moulded and solution-cast PVDF/Li–AHA composites. It is evident that the polar phase fraction consistently rises with increasing Li–AHA concentration in both the compression-moulded and solution-cast PVDF/Li–AHA composite films. Notably, solution-cast neat PVDF films exhibit ~35% polar phase formation, whereas their compression-moulded counterparts show ~32% polar phase formation. Moreover, solution-cast PVDF/Li–AHA composite films with a 15 wt% Li–AHA concentration demonstrate ~60% polar phase, whereas the corresponding compression-moulded composite films exhibit ~49% polar phase, which is attributed to the increased hydrogen bonding between the –NH functional moiety of Li–AHA and fluorine moiety of PVDF dipoles leading to higher electroactive phase contents in the PVDF/Li–AHA composites, as previously observed *via* FTIR spectroscopy. The higher electronegativity of fluorine in PVDF compared to nitrogen in the amine group drives this interfacial interaction, resulting in the generation of additional dipoles, thereby further augmenting the polar phase content in the PVDF/Li–AHA composites.[47] Also, as mentioned earlier, dipolar interactions and hydrogen bonding between the PVDF moieties and DMF molecules contribute to a more organized arrangement of CH_2–CF_2 dipoles, promoting the formation of the *trans* (TTT) conformation, which represents the electroactive phases. This combined effect leads to a higher polar phase fraction in PVDF for solution-cast composites compared to compression-moulded samples.

3.4. Analysis of the piezoelectric coefficient *via* piezoelectric force microscopy (PFM)

Piezoelectric properties of neat PVDF and PVDF/Li–AHA composites were investigated *via* a PFM study in contact mode. The PFM tip is a conductive probe, which scans across the sample surface at an applied AC voltage. This causes small deformations at the molecular level in the composite film. The cantilever tip detects the deformation to produce the output. Due to the principle of the inverse piezoelectric effect, the tip then bends when voltage is applied, and this movement is reciprocated to

create an image.[46] The deformation is thus recorded as the amplitude with applied bias voltage.

It is observed (Fig. 5) that there is an increase in amplitude (Fig. 5(a) and (b)) and the corresponding d_{33} values (piezoelectric coefficient) (Fig. 5(c)) of the PVDF/Li–AHA composite with an increase in Li–AHA concentration in compression-moulded as well as solution-cast films. The observed amplitude signifies the magnitude of polarization in the PVDF/Li–AHA composites. A maximum amplitude of ~240 nm and ~260 nm was obtained in the case of the PVDF/Li–AHA composite with 15 wt% Li–AHA prepared *via* compression-moulding and solution-casting, respectively (Fig. 5(a) and (b)). The d_{33} value were ~63 pm V^{-1} and ~72 pm V^{-1} in the compression-moulded and solution-cast PVDF/Li–AHA composites with 15 wt% of Li–AHA (Fig. 5(c)). Increased interfacial interaction, resulting in a greater proportion of polar phase generation, can be attributed for an increased d_{33} value at higher concentrations of Li–AHA in PVDF/Li–AHA composites. Once again, the higher d_{33} value in solution-cast PVDF/Li–AHA composite samples compared to the corresponding composite film prepared *via* compression-moulding is attributed to the formation of a larger amount of polar phase in the solution-cast sample.

3.5. Ferroelectric properties *via* polarization *vs.* electric field

The polarization curves with varying electric fields for compression-moulded and solution-cast neat PVDF and PVDF/Li–AHA composites were obtained to investigate the ferroelectric behaviour of PVDF/Li–AHA composites under an electric field. The hysteresis loops were recorded at 50 Hz and at an applied voltage of 1000 V, which are shown in Fig. 6(a) and (b). Fig. S4 (ESI†) shows the hysteresis loops of compression-moulded and solution-cast PVDF/Li–AHA composites of all the compositions. The hysteresis loops shown in Fig. 6 and Fig. S4 (ESI†) show unsaturated PE-loop curves and lack the characteristic curved shape seen in ideal ferroelectric materials.

It is understood that the ferroelectric properties of PVDF are entirely reliant on the quantity of electroactive phases present in PVDF matrix. PVDF/Li–AHA composites exhibit enhanced ferroelectric properties compared to neat PVDF, in the case of both compression-moulded and solution-cast films. Neat PVDF shows a weak P–E loop, but compression-moulded and solution-cast PVDF/Li–AHA composites films of 15 wt% Li–AHA exhibit maximum polarization (P_{max}) values of ~0.014 μC cm^{-2} and ~0.07 μC cm^{-2}, respectively (Fig. 6(a) and (b)). It is also observed that remnant polarization (P_r) and maximum polarization increase progressively in the PVDF/Li–AHA composite with an increase in the Li–AHA concentration in both compression-moulded as well solution-cast films. The improved ferroelectric properties can be attributed to larger polar phases in the PVDF/Li–AHA composites. PVDF/Li–AHA composite films contain ferroelectric domains, which become

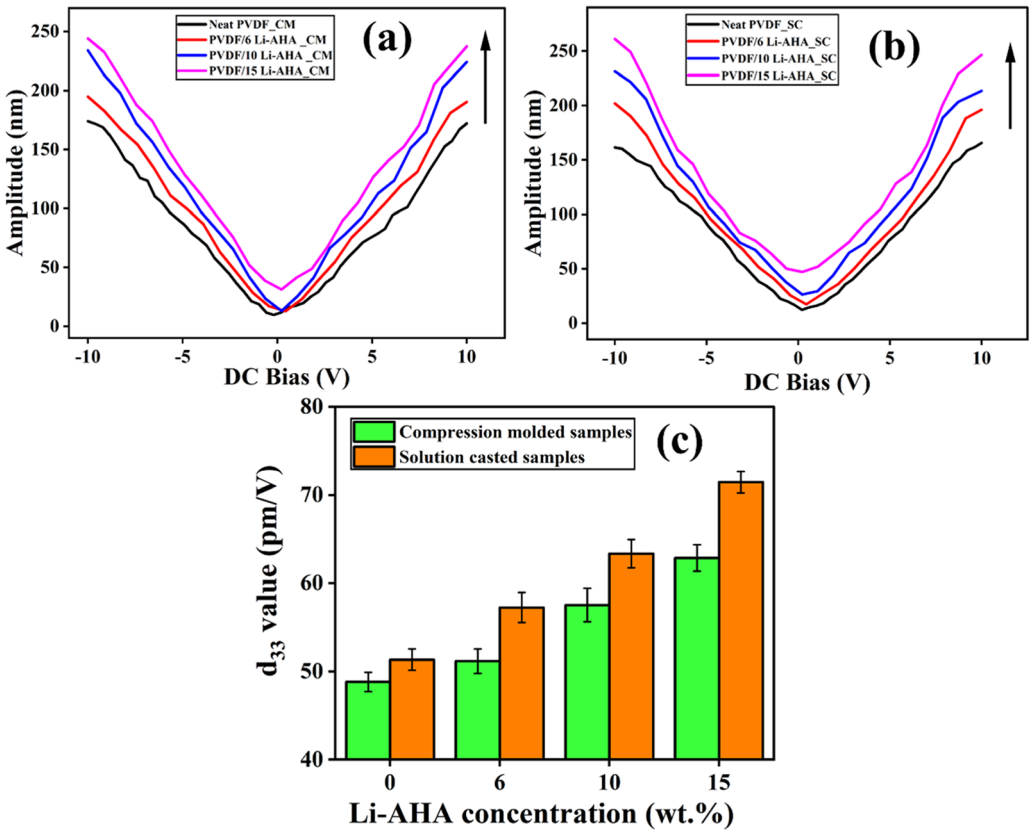

Fig. 5 Variation of amplitude with bias voltage in (a) compression-moulded pure PVDF and PVDF/Li–AHA composite films and (b) solution-cast pure PVDF and PVDF/Li–AH composite films and (c) a comparison of the d_{33} values of compression-moulded and solution-cast PVDF/Li–AHA composite films with varying Li–AHA concentration.

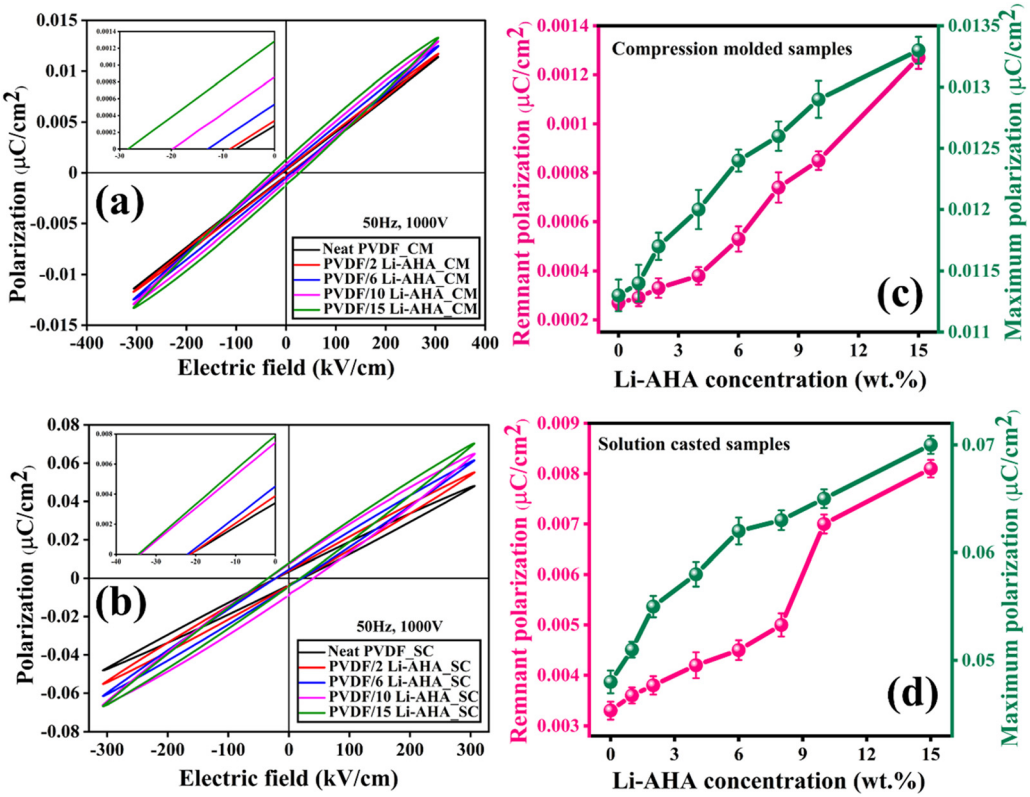

Fig. 6 Polarization *versus* electric field loops of PVDF/Li–AHA composites prepared by (a) compression-moulding and (b) solution-casting, (c) and (d) variation of remnant polarization and maximum polarization with varying Li–AHA concentration in PVDF/Li–AHA composites prepared *via* (c) compression-moulding and (d) solution-casting, respectively.

oriented with the increase in electric field, which is further enhanced with the increase in polar phase content in the PVDF/Li–AHA composites.[45] Further, the breakdown voltages of compression-moulded and solution-cast PVDF/Li–AHA composites of 15 wt% Li–AHA were observed to be ~4200 V and ~5000 V, respectively, whereas neat PVDF films could reach only up to ~1700 V.

The change of remnant polarization (P_r) and maximum polarization (P_{max}) of PVDF and PVDF/Li–AHA composites, varying with Li–AHA concentration, are illustrated in Fig. 6(c) and (d). Solution-cast PVDF/Li–AHA composite samples exhibit slightly higher polarization values compared to their compression-moulded counterparts, due to greater polar phase fractions. The PVDF/Li–AHA composite of 15 wt% Li–AHA shows the highest P_r and P_{max} values due to significantly enhanced interfacial interactions resulting in a higher polar phase fraction. Due to strong interfacial interactions (H-bonding) between $-CF_2$ dipoles and $-NH_2$ groups of Li–AHA, polarization occurs which leads to an increase in remnant polarization.[48]

To explore the ferroelectric properties of our samples, we conducted additional measurements using piezoresponse force microscopy (PFM). PFM is a highly sensitive method for detecting nanoscale ferroelectric domains and switching behaviour that may be missed in macroscopic hysteresis loops due to factors like low electric field strength, sample defects, or suboptimal conditions. By visualizing the domains and their reaction to applied fields, PFM provides clearer evidence of ferroelectricity, even when macroscopic measurements do not show saturation. It also allows us to differentiate between ferroelectric and dielectric responses through quantitative analysis of piezoresponse amplitude and phase.

3.6. Piezoelectric energy harvesting device

To showcase the energy harvesting capability of the devices, a vertical compressive force generated by human finger tapping was applied on the fabricated devices. The resulting output voltage was logged with an oscilloscope, both for the compression-moulded and solution-cast films, as depicted in Fig. S5 (ESI†), and the circuit model of the nanogenerator is also presented in Fig. 7(a). Fig. S5 (ESI†) also depicts the variation of the force of ~12–15 N, which was applied as a function of time on the device. While pressing, the bound charges initiate a potential within the nanogenerator. Consequently, external charges are attracted to the nanogenerator to neutralize this potential difference. Upon releasing the force, the piezopotential decreases, causing the accumulated free charges to generate an opposing potential at the two surfaces of the device. The positive amplitude of output voltage corresponds to the 'press' of the impulse, whereas the negative amplitude reflects the 'release' of the impulse during finger tapping.[49]

The output voltage signal from the respective compression-moulded and solution-cast PVDF/Li–AHA composite films is

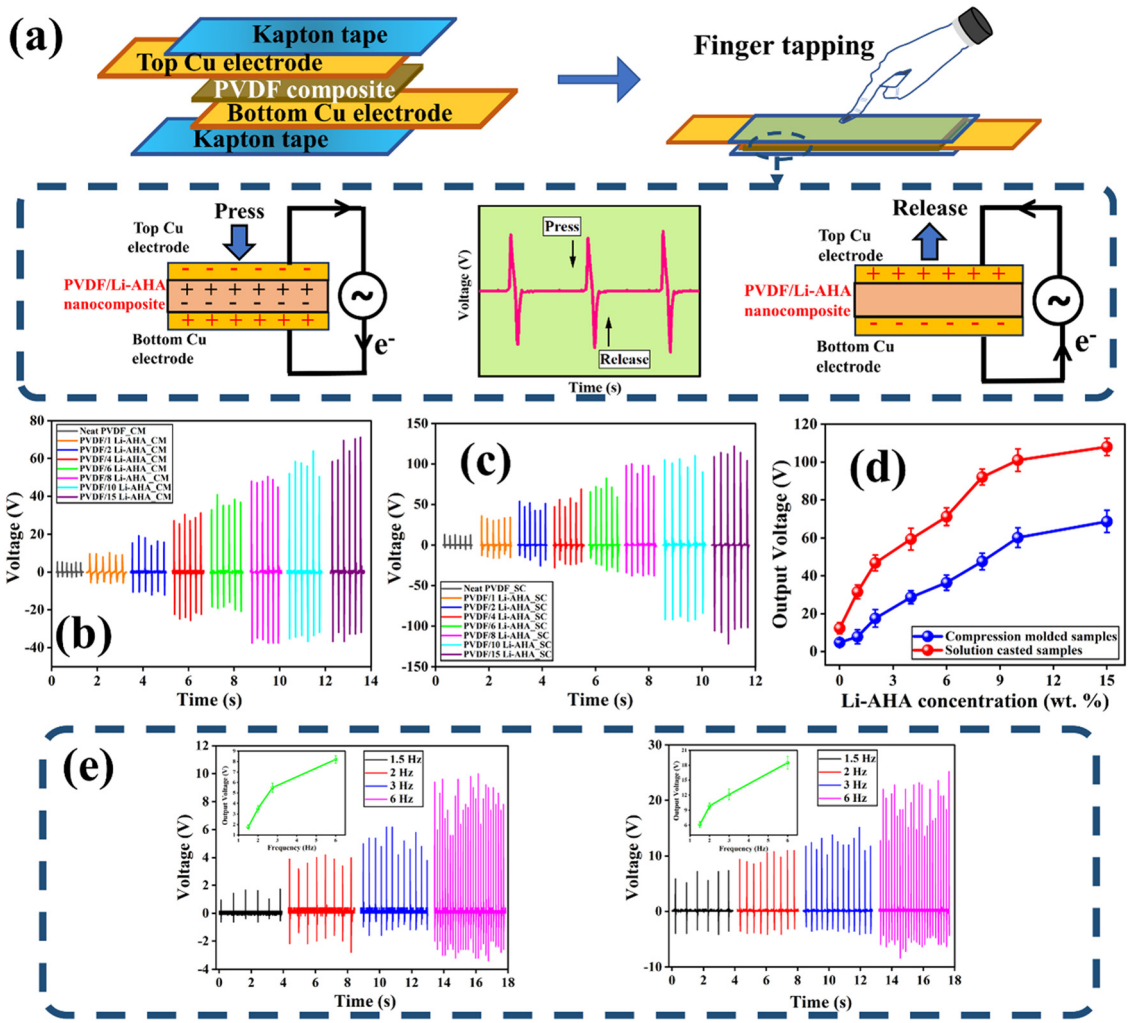

Fig. 7 (a) A schematic representation showing the working principle of the nanogenerator, (b) and (c) output voltage obtained by finger tapping on the PVDF/Li–AHA composite-based energy harvesting devices prepared by (b) compression-moulded films and (c) solution-cast films, (d) comparison of output voltage in compression-moulded and solution-cast films of neat PVDF and PVDF/Li–AHA composites, and (e) variation of output voltage for different frequencies during the finger tapping experiment in compression-moulded and solution-cast PVDF/Li–AHA composites of 15 wt% Li–AHA, respectively.

shown in Fig. 7(b) and (c). The corresponding recorded piezoelectric output voltage of the PVDF/Li–AHA composite with varying concentration of Li–AHA is depicted in Fig. 7(d) for compression-moulded and solution-cast films. During the impact and release of force, the polarization of the piezoelectric charge becomes disturbed, thus creating a potential imbalance in the two electrodes, which causes the electrons to flow in the circuit.[50,51] Due to this, alternate positive and negative voltages are generated in a short time span. In both the systems, the output piezoelectric response increases in the PVDF/Li–AHA composite as the concentration of Li–AHA increases. The device prepared with the neat PVDF film generated an output of ~10.7 ± 0.6 V in the case of the solution-cast film and ~5.2 ± 0.4 V in the case of compression-moulded film. Further, the output response increases with the increase in the Li–AHA concentration in the PVDF/Li–AHA composite device, and a maximum output voltage of ~60.8 ± 0.3 V and ~110.7 ± 0.5 V was obtained in the PVDF/Li–AHA composite of 15 wt% Li–AHA for compression-moulded and solution-cast films, respectively. Moreover, a maximum output voltage of ~18.2, ~28.1, ~37.5, ~42.3 and ~58.1 V was obtained in the case of the device fabricated with the compression-moulded PVDF/Li–AHA composite of 2, 4, 6, 8 and 10 wt% of Li–AHA. Whereas a maximum output voltage of ~47.4, ~59.6, ~68.2, ~91.8 and ~101.4 V was obtained in the case of device fabricated with the solution-cast PVDF/Li–AHA composite of 2, 4, 6, 8 and 10 wt% of Li–AHA. A higher piezo-voltage response obtained in the PVDF/Li–AHA composites can be attributed to a higher fraction of the polar phase of PVDF, compared to neat PVDF films. The increased piezo-voltage response of solution-cast PVDF/Li–AHA composite as compared to the compression-moulded composite is due to the more electroactive phase of PVDF, which leads to the creation of dipoles in the composite. In general, with an increase in the concentration of Li–AHA in the PVDF/Li–AHA composite films, interfacial interaction is greatly enhanced, which results in the improved electromechanical response in

the composite. Due to the higher piezoelectric output voltage in PVDF/Li–AHA composites, the devices can be exploited for energy harvesting.[52]

To assess the impact of frequency on the output voltage of the fabricated device, the frequency of finger tapping was adjusted from 1 to 6 Hz to simulate low frequency motions.[53] The output voltage of the compression-moulded and solution-cast PVDF/Li–AHA composite device of 15 wt% Li–AHA with varying frequency is represented in Fig. 7(e). The output voltage increases with tapping frequency from 1 Hz to 6 Hz, with the solution-cast composite sample displaying a superior response compared to the compression-moulded film. This can be attributed to better impedance matching with the digital oscilloscope, resulting in higher electrical outputs. The internal impedance of the device decreases with increasing frequency, leading to improved coherency of the fabricated device's internal electrical impedance and the oscilloscope, thereby increasing the output voltage. The effective response to low-frequency indicates that the fabricated device holds the potential for harvesting energy from low-frequency motions, such as human movements.[49,54]

Further, the composite device was tested under the biomechanical stimulation of knuckle tapping, wrist tapping, fist thumping, little finger tapping, and keyboard typing. Fig. 8 depicts the output voltages obtained for various tapping motions on the devices fabricated from the PVDF/Li–AHA composite of 15 wt% Li–AHA made *via* compression-moulding and solution-casting. Each type of tapping generates a different amount of force on the device, and it is evident that even with a gentle touch, the device is sensitive enough to generate a voltage. The significant response of the nanogenerator to human motions demonstrates its potential to effectively harvest energy from various human movements.[54]

To determine the power density of PVDF/Li–AHA composites, varying resistors (10 kΩ to 200 MΩ) were connected in series with the device, and the voltage drop across the resistors was simultaneously measured as shown in Fig. 9(a). The fabricated composite device of 15 wt% Li–AHA has been used for further piezoelectric performance analysis as this sample depicted the highest voltage response among all the other composites. The output power density (P_d) was calculated using

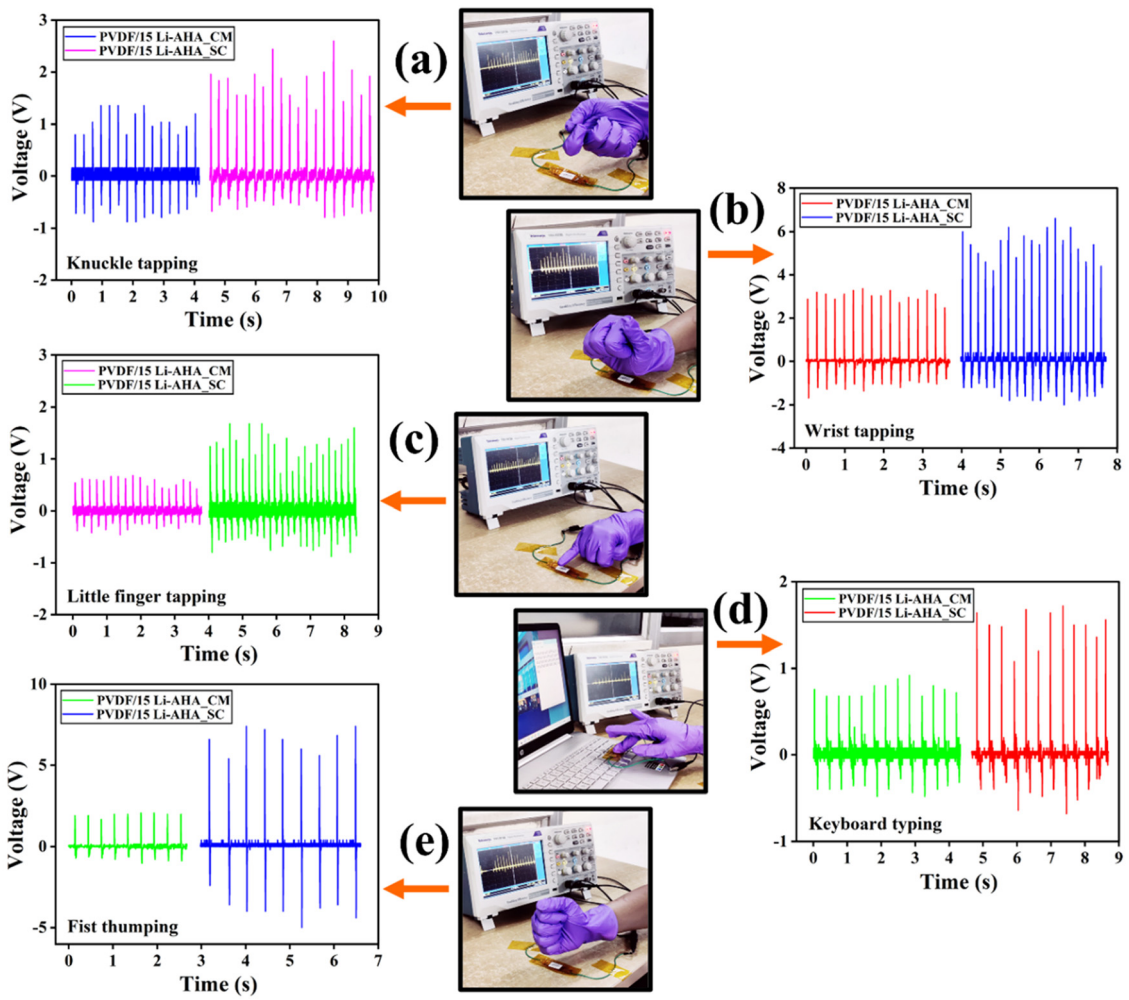

Fig. 8 Variation of output voltage in case of compression-moulded and solution-cast PVDF/Li–AHA composite films of 15 wt% Li–AHA in case of (a) knuckle tapping, (b) wrist tapping, (c) little finger tapping, (d) keyboard tapping, and (e) fist thumping.

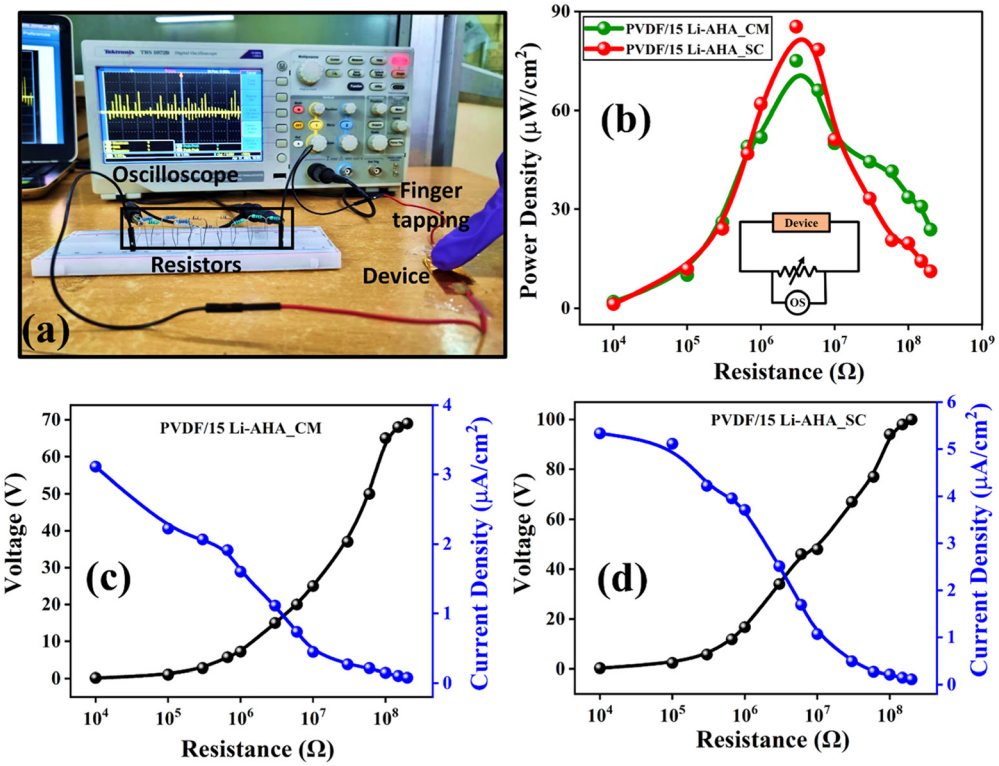

Fig. 9 (a) An image showing the electrical set-up with different resistors and device, (b) the variation of power density with increasing load resistance for compression-moulded and solution-cast PVDF/Li–AHA composites of 15 wt% Li–AHA, (c) and (d) the variation of load current with increasing load resistance for (c) compression-moulded PVDF/Li–AHA composite film and (d) solution-cast PVDF/Li–AHA composite film of 15 wt% Li–AHA.

eqn (3):

$$P_d = \frac{V_L^2}{AR_L} \quad (3)$$

where, A is the effective electrode area of the fabricated device and V_L is the voltage drop across applied load resistance R_L. Fig. 9(b) shows the variation of calculated power density across varying load resistors for compression-moulded and solution-cast composite devices. A maximum power density of ~75 μJ cm^{-2} was obtained from the device made *via* compression-moulding. Interestingly, a much higher power density of ~85 μJ cm^{-2} was obtained from the device made *via* solution-casting (Fig. S6, ESI†). This is due to the higher output voltage obtained from solution-cast film (~110 V) as compared to the corresponding compression-moulded film (~60 V).

The load current across the resistance (R_L) can be calculated from power (P) using eqn (4) and is mapped as a function of varying resistance in Fig. 9(c) and (d):

$$I = \sqrt{\frac{P}{R_L}} \quad (4)$$

The maximum current density obtained in the case of compression-moulded and solution-cast PVDF/Li–AHA composite film of 15 wt% Li–AHA was 3.1 μA cm^{-2} and 5.3 μA cm^{-2}, respectively.

In order to further demonstrate that our device has potential applications in energy harvesting, various capacitors (with different capacitance) were charged by finger tapping. Different capacitors of 1 μF, 2.2 μF and 4.7 μF were connected to the device individually using the bridge rectifier (Fig. 10(a)). The charging–discharging behaviour of the capacitors for compression-moulded and solution-cast PVDF/Li–AHA composite films of 15 wt% Li–AHA are shown in Fig. 10(b) and (c), respectively. The highest voltage of ~1.92 V for the 1 μF capacitor was obtained within a short time span of ~50 s for the solution-cast PVDF/Li–AHA composite device. The highest voltage of ~0.92 V for the 1 μF capacitor was obtained within a very short time span of ~40 s for the device made *via* the compression-moulded PVDF/Li–AHA composite film. Fig. 10(d) depicts the comparison of charging voltage across the three different capacitors in the case of compression-moulded and solution-cast PVDF/Li–AHA composite films of 15 wt% Li–AHA. The higher value of charging voltage in the case of the solution-cast composite films can be attributed to the higher polar phase fraction as compared to the compression-moulded composite films.[54]

The stored energy (E) in the capacitor of capacitance C was calculated using eqn (5), which is depicted in Fig. 10(e):

$$E = \frac{CV^2}{2} \quad (5)$$

where, V is the saturation voltage up to which the capacitor (C) can be charged.

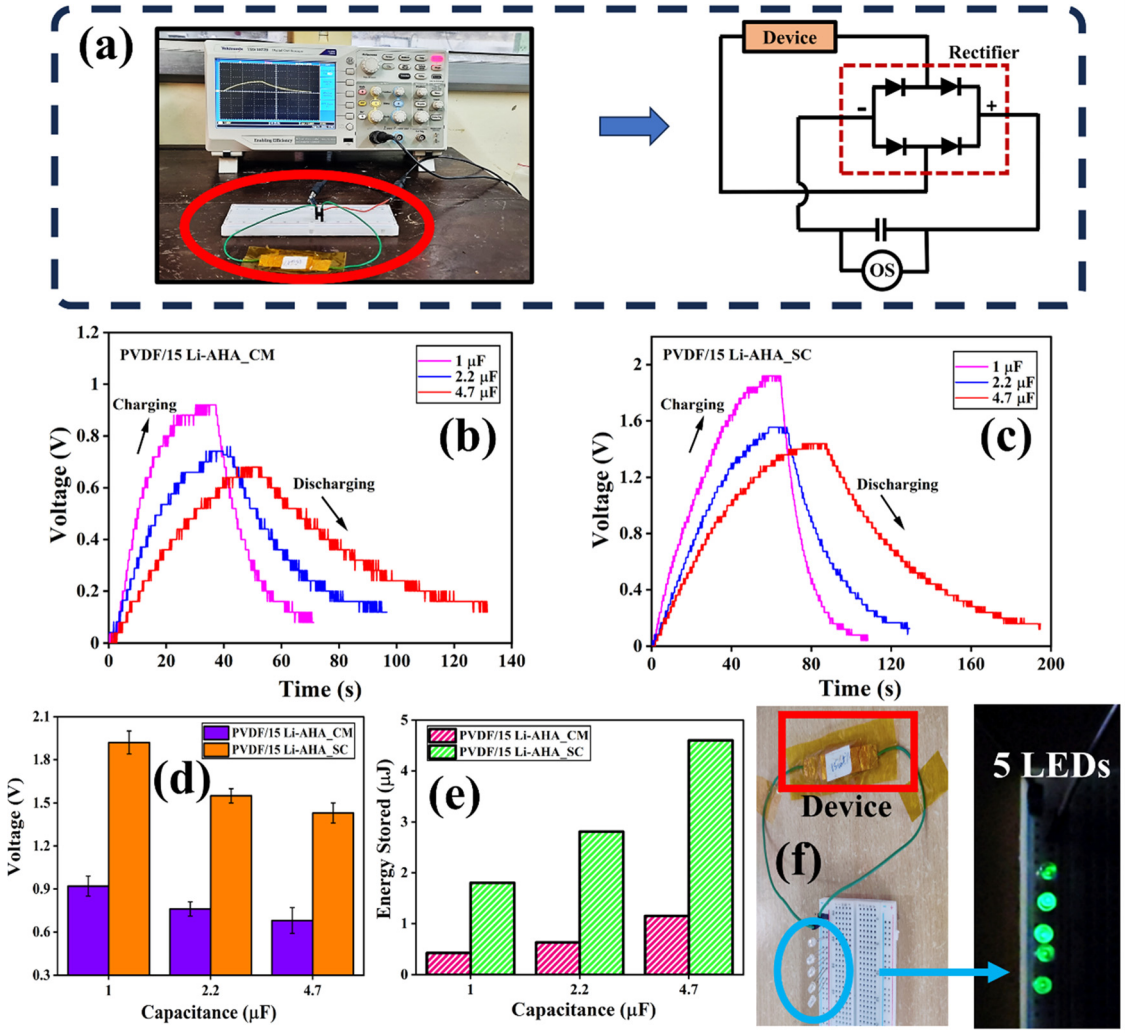

Fig. 10 (a) Image and circuit diagram showing the set-up with capacitors and rectifier, (b) and (c) charging and discharging curves with three different capacitors for the device made *via* (b) compression-moulded, and (c) solution-cast PVDF/Li–AHA composites of 15 wt% Li–AHA, (d) a comparison of the charging voltages for three different capacitors, (e) a comparison of the energy stored for three different capacitors by the devices made *via* compression-moulding and solution-casting of PVDF/Li–AHA composites of 15 wt% Li–AHA, and (f) an image showing the LED circuit and lighting up of 5 LEDs with finger tapping on the device made with the solution-cast PVDF/Li–AHA composite of 15 wt% Li–AHA concentration.

To calculate maximum stored energy, the maximum capacitor of 4.7 μF and the respective maximum voltage stored in it was considered, in the case of both compression-moulded and solution-cast composite devices. The maximum stored energy was determined to be ~1.1 μJ and ~4.6 μJ in compression-moulded and solution-cast PVDF/Li–AHA composite films of 15 wt% Li–AHA, respectively. Hence, it is evident that the capacitors can be charged within a short time span, which makes them a promising candidate for powering tiny portable electronic gadgets.

To show the efficiency of our devices, we lit up five LEDs using our device by finger tapping on the device made *via* solution-cast PVDF/Li–AHA composite film of 15 wt% Li–AHA, as shown in Fig. 10(f) and the supporting Video SV (ESI†). A video was taken for 10 s of lighting up the LEDs by applying an external force *via* hand tapping, and the snapshots were taken from the video at intervals of 0.1 second (frame rate: 30 frames per s) with the help of the software, as depicted in Fig. 10(f).

4. Conclusions

PVDF/Li–AHA composites were produced through melt-mixing, with varying Li–AHA concentrations ranging from 1–15 wt%, aimed at establishing strong interfacial interaction (hydrogen bonding) between $-CF_2$ groups of PVDF and the NH_2 moiety of Li–AHA. Following melt-mixing, solution-casting and compression-moulding techniques were employed to create PVDF/Li–AHA composite thin films, allowing investigation into the effects of compression-moulding and solution-casting on the structure and ferroelectric and piezoelectric properties of the composites.

Observations of the morphological analysis indicated a reduction in the average spherulite size in PVDF with increasing Li–AHA concentration in both compression-moulded and solution-cast PVDF/Li–AHA composites. Notably, solution-cast composite films exhibited significantly smaller average spherulite sizes compared to their compression-moulded counterparts,

suggesting the heterogeneous nucleating effect of Li–AHA during PVDF crystallization.

FTIR spectroscopic analysis revealed hydrogen bonding between the $-CF_2$ dipoles of PVDF and NH_2 functionality of Li–AHA in PVDF/Li–AHA composites. Shifts in the –NH peaks of Li–AHA functional groups were observed, indicating that the interaction strength changes with varying the Li–AHA concentration. Additionally, progressive shifts in the $\nu_s(CF_2)$ band with increasing Li–AHA concentration suggested enhanced H-bonding between the $-NH_2$ moieties of Li–AHA and $-CF_2$ of PVDF.

Further analysis by FTIR spectroscopy and WAXD analysis confirmed the role of Li–AHA in influencing polar phase evolution of PVDF in both compression-moulded and solution-cast composites. Solution-cast composites exhibited a higher polar phase fraction ($\sim$60%) compared to compression-moulded composites ($\sim$49%) with 15 wt% Li–AHA, which is attributed to the improved H-bonding interactions between Li–AHA and PVDF chains.

Moreover, a higher d_{33} value ($\sim$72 pm V^{-1}) was achieved in solution-cast PVDF/Li–AHA composites with 15 wt% Li–AHA compared to the corresponding compression-moulded composite ($\sim$63 pm V^{-1}). The enhanced d_{33} value in the solution-cast films was attributed to the greater extent of the polar phase evolution. Ferroelectric properties showed increased remnant polarization values with Li–AHA addition in both compression-moulded and solution-cast composite films, with marginally higher values observed in solution-cast films due to their increased electroactive phase content.

Sensor devices were fabricated using solution-cast and compression-moulded PVDF/Li–AHA composite films with 15 wt% Li–AHA. Output voltages of $\sim$60 V and $\sim$110 V were obtained from devices fabricated from compression-moulded and solution-cast PVDF/Li–AHA composite films of 15 wt% Li–AHA, respectively. A maximum power density of $\sim$75 μJ cm^{-2} and $\sim$85 μJ cm^{-2} was obtained from devices made from compression-moulded and solution-cast PVDF/Li–AHA composite films, respectively, with 15 wt% Li–AHA. For the 4.7 μF capacitor, stored energy density of $\sim$1 μJ cm^{-2} and $\sim$4.8 μJ cm^{-2} was obtained from compression-moulded and solution-cast composite film of 15 wt% Li–AHA, respectively. Also, five LEDs were lit up using our device by finger tapping on the device made *via* the solution-cast PVDF/Li–AHA composite film of 15 wt% Li–AHA, which further shows the efficiency of the fabricated nanogenerator device.

In brief, an interrelationship was established between the processing methods, the evolution of crystalline structures and the resultant piezoelectric properties in PVDF/Li–AHA composite films. A piezoelectric energy harvesting device was successfully fabricated using PVDF/Li–AHA composite films, which can be utilized for various bio-mechanical motions.

Author contributions

Ananya Aishwarya: conceptualization, methodology, investigation, writing – original draft. Akanksha Adaval: investigation, writing – review. Suvankar Mondal: investigation. Titas Dasgupta: writing – review & editing. Arup R. Bhattacharyya: supervision, conceptualization, writing – review & editing.

Data availability

Data will be available on request.

Conflicts of interest

The authors declare no conflict of research interest or competing financial interest.

Acknowledgements

The authors would like to acknowledge the SAIF and CRNTS facilities, IIT Bombay for providing the FTIR facility and AFM facility. The authors would also like to acknowledge the Department Central Facilities at MEMS, IIT Bombay for X-ray diffraction and piezo-force microscopy.

References

1 R. H. Kim, D. H. Kim and J. Xiao, Waterproof AlInGaP optoelectronics on stretchable substrates with applications in biomedicine and robotics, *Nat. Mater.*, 2010, **9**, 929–937, DOI: **10.1038/nmat2879**.

2 A. George, H. Varghese, A. Chandran, K. P. Surendran and E. B. Gowd, Directional freezing-induced self-poled piezoelectric nylon 11 aerogels as high-performance mechanical energy harvesters, *J. Mater. Chem. A*, 2024, **12**, 911–922, DOI: **10.1039/D3TA05911A**.

3 B. C. Sekhar, B. Dhanalakshmi, B. S. Rao, S. Ramesh, K. V. Prasad, P. S. V. Subba Rao and B. P. Rao, Piezoelectricity and its applications, *Ferroelectr. Mater.*, 2021, 1–33, DOI: **10.5772/intechopen.96154**.

4 S. Mondal, S. Thakur, S. Maiti, S. Bhattacharjee and K. K. Chattopadhyay, Self-Charging Piezo-Supercapacitor: One-Step Mechanical Energy Conversion and Storage, *ACS Appl. Mater. Interfaces*, 2023, **15**(6), 8446–8461, DOI: **10.1021/acsami.2c17538**.

5 T. Takahashi, K. Takei, A. G. Gillies, R. S. Fearing and A. Javey, Carbon Nanotube Active-Matrix Backplanes for Conformal Electronics and Sensors, *Nano Lett.*, 2011, **11**(12), 5408–5413, DOI: **10.1021/nl203117h**.

6 J. Sirohi and I. Chopra, Fundamental understanding of piezoelectric strain sensors, *Intell. Mater. Sys. Struct.*, 2000, **11**, 246–257, DOI: **10.1106/8BFB-GC8P-XQ47-YC**.

7 S. Mishra, L. Unnikrishnan, S. K. Nayak and S. Mohanty, Advances in Piezoelectric Polymer Composites for Energy Harvesting Applications: A Systematic Review, *Macromol. Mater. Eng.*, 2018, 1800463, DOI: **10.1002/mame.201800463**.

8 A. J. Lovinger, Poly(Vinylidene fluoride) Development in Crystalline Polymers, *Appl. Sci.*, 1982, 195–261, DOI: **10.1007/978-94-009-7343-5_5**.

9 A. Aliane, M. Benwadih, B. Bouthinon, R. Coppard, F. D. Santos and A. Daami, Impact of crystallization on ferro-, piezo- and pyro-electric characteristics in thin film P(VDF-TrFE), *Org. Electron.*, 2015, **25**, 92–98, DOI: **10.1016/j.orgel.2015.06.007**.
10 J. H. Bae and S. H. Chang, Characterization of an electroactive polymer (PVDF-TrFE) film-type sensor for health monitoring of composite structures, *Compos. Struct.*, 2015, **131**, 1090–1098, DOI: **10.1016/j.compstruct.2015.06.075**.
11 W. C. Gan, W. H. A. Majid and T. Furukawa, Ferroelectric polarization, pyroelectric activity and dielectric relaxation in Form IV poly(vinylidene fluoride), *Polymer*, 2016, **82**, 156–165, DOI: **10.1016/j.polymer.2015.11.024**.
12 K. Asai, M. Okamoto and K. Tashiro, Polymer Communication Real-time investigation of crystallization in poly(vinylidene fluoride)-based nano-composites probed by infrared spectroscopy, *Polymer*, 2018, **49**, 5186–5190, DOI: **10.1016/j.polymer.2008.09.061**.
13 A. N. Arshad, M. H. M. Wahid, M. Rusop, W. H. A. Majid, R. H. Y. Subban and M. D. Rozana, Dielectric and Structural Properties of Poly(vinylidene fluoride) (PVDF) and Poly(vinylidene fluoride-trifluoroethylene) (PVDF-TrFE) Filled with Magnesium Oxide Nanofillers, *J. Nanomater*, 2019, 5961563, DOI: **10.1155/2019/5961563**.
14 R. Hasegawa, Y. Takahashi, Y. Chatani and H. T. Adokoro, Crystal Structures of Three Crystalline Forms of Poly(vinylidene fluoride), *Polym. J.*, 1972, **3**(5), 600–606, DOI: **10.10.1295/polymj.3.600**.
15 H. Kawai, The Piezoelectricity of Poly(vinylidene Fluoride), *Jpn. J. Appl. Phys.*, 1969, **8**(7), 975–976, DOI: **10.1143/JJAP.8.975**.
16 N. G. McCrum, B. E. Read and G. Williams, Anelastic and dielectric effects in polymeric solids, *J. Appl. Polym. Sci.*, 1969, **13**(2), 397.
17 M. Wegener, W. Künstler and R. Gerhard-Multhaupt, Piezo-, pyro- and ferroelectricity in poly(vinylidene fluoride- hexafluoropropylene) copolymer films, *Integr. Ferroelectr.*, 2004, **60**, 111–116, DOI: **10.1080/10584580490441764**.
18 G. Guerra, F. E. Karasz and W. J. MacKnight, On blends of Poly(vinylidene Fluoride) and Poly(vinyl Fluoride), *Macromolecules*, 1986, **19**(2), 3091.
19 C. P. Wong, *Polymers for electronic and photonic applications*. 1993, p. 661.
20 P. Martins, A. C. Lopes and S. Lanceros-Mendez, Electroactive phases of poly(vinylidene fluoride): Determination, processing and applications, *Prog. Polym. Sci.*, 2014, **4**(39), 683–706, DOI: **10.1016/j.progpolymsci.2013.07.006**.
21 M. Bohlen and K. Bolton, Inducing the β-phase of poly(vinylidene fluoride): a review, *Ann. Rev. Nanosci. Nanotechol.*, 2014, **1**, 1.
22 A. Salimi and A. Yousefi, Analysis method: FTIR studies of β-phase crystal formation in stretched PVDF films, *Polym. Test*, 2003, **22**, 699–704, DOI: **10.1016/S0142-9418(03)00003-5**.
23 B. Mohammadi, A. A. Yousefi and S. M. Bellah, Effect of tensile strain rate and elongation on crystalline structure and piezoelectric properties of PVDF thin films, *Polym. Test.*, 2007, **26**, 42–50, DOI: **10.1016/j.polymertesting.2006.08.003**.
24 V. Sencadas, M. V. Moreira, S. Lanceros-Méndez, A. S. Pouzada and R. Gregório Filho, α-to β Transformation on PVDF Films Obtained by Uniaxial Stretch, *Mater. Sci. Forum*, 2006, **514–516**, 872–876, DOI: **10.4028/www.scientific.net/MSF.514-516.872**.
25 T. Kaura, R. Nath and M. Perlman, Simultaneous stretching and corona poling of PVDF films, *J. Phys. D: Appl. Phys.*, 1991, **24**, 1848, DOI: **10.1088/0022-3727/24/10/020**.
26 M. Sharma, G. Madras and S. Bose, Process induced electroactive β-polymorph in PVDF: effect on dielectric and ferroelectric properties, *Phys. Chem. Chem. Phys.*, 2014, **16**, 14792–14799, DOI: **10.1039/C4CP01004C**.
27 A. Gebrekrstos, M. Sharma, G. Madras and S. Bose, New Physical Insights into Shear History Dependent Polymorphism in Poly-(vinylidene fluoride), *Cryst. Growth Des.*, 2016, **16**, 2937–2944, DOI: **10.1021/acs.cgd.6b00282**.
28 J. Zheng, A. He, J. Li and C. C. Han, Polymorphism control of poly(vinylidene fluoride) through electrospinning, *Macromol. Rapid Commun.*, 2007, **28**, 2159–2162, DOI: **10.1002/marc.200700544**.
29 R. P. Vijayakumar, D. V. Khakhar and A. Misra, Phase transformation and enhancement of toughness in polyvinylidene fluoride by onium salts, *J. Polym. Sci., Part B: Polym. Phys.*, 2011, **49**(18), 1339–1344, DOI: **10.1002/polb.22303**.
30 C. Xing, M. Zhao, L. Zhao, J. You, X. Cao and Y. Li, Ionic liquid modified poly(vinylidene fluoride): crystalline structures, miscibility, and physical properties, *Polym. Chem.*, 2013, **4**, 5726–5734, DOI: **10.1039/C3PY00466J**.
31 S. Jana, S. Garain, S. Sen and D. Mandal, The influence of hydrogen bonding on the dielectric constant and the piezoelectric energy harvesting performance of hydrated metal salt mediated PVDF films, *Phys. Chem. Chem. Phys.*, 2015, **17**, 17429–17436, DOI: **10.1039/C5CP01820J**.
32 J. Banerjee, A. S. Panwar, K. Mukhopadhyay, A. K. Saxena and A. R. Bhattacharyya, Deagglomeration of multi-walled carbon nanotubes *via* an organic modifier: structure and mechanism, *Phys. Chem. Chem. Phys.*, 2015, **17**, 25365–25378, DOI: **10.1039/C5CP03736K**.
33 J. Li, C. Zhao, K. Xia, X. Liu, D. Li and J. Han, Enhanced piezoelectric output of the PVDF-TrFE/ZnO flexible piezoelectric nanogenerator by surface modification, *Appl. Surf. Sci.*, 2019, **463**, 626–634, DOI: **10.1016/j.apsusc.2018.08.266**.
34 A. Salimi and A. A. Yousefi, Conformational changes and phase transformation mechanisms in PVDF solution-cast films, *J. Polym. Sci., Part B: Polym. Phys.*, 2004, **42**(18), 3487–3495, DOI: **10.1002/polb.20223**.
35 A. Gradys, P. Sajkiewicz, S. Adamovsky, A. Minakov and C. Schick, Crystallization of poly(vinylidene fluoride) during ultra-fast cooling, *Thermochim. Acta*, 2007, **461**(1–2), 153–157, DOI: **10.1016/j.tca.2007.05.023**.
36 T. Arumugham, N. J. Kaleekkal, D. Rana and K. I. Sathiyanarayanan, PFOM fillers embedded PVDF/cellulose dual-layered membranes with hydrophobic–hydrophilic channels for desalination *via* direct contact membrane

distillation process, *RSC Adv.*, 2019, **9**, 41462–41474, DOI: 10.1039/C9RA08945D.

37 M. F. H. A. El-Kader, N. S. Awwad, H. A. Ibrahium and M. K. Ahmed, Graphene oxide fillers through polymeric blends of PVC/PVDF using laser ablation technique: electrical behavior, cell viability, and thermal stability, *J. Mater. Res. Technol.*, 2021, **13**, 1878–1886, DOI: 10.1016/j.jmrt.2021.05.024.

38 A. Adaval, I. Chinya, B. B. Bhatt, S. Kumar, D. Gupta, I. Samajdar, M. Aslam, T. W. Turney, G. P. Simon and A. R. Bhattacharyya, Poly(vinylidene fluoride)/graphene oxide composites for piezoelectric applications: Processing, structure, dielectric and ferroelectric properties, *Nano-Struct. Nano-Objects*, 2022, 31, DOI: 10.1016/j.nanoso.2022.100899.

39 H. Zhang, M. Xu, M. Chen, Y. Cui, L. Chen, X. Dai and J. Dai, Fabrication of high flux porphrin-cored with siloxane-poly(amido amine) dendrimer/PVDF composite membrane for oil/water separation and dye degradation, *J. Environ. Chem. Eng.*, 2022, **10**(3), 107634, DOI: 10.1016/j.jece.2022.107634.

40 M. S. Gopika and B. Bindhu, Modified molybdenum disulfide induced beta polymorph phase transition in Polyvinylidene fluoride, *Chem. Phys. Lett.*, 2020, **740**, 137081, DOI: 10.1016/j.cplett.2019.137081.

41 E. Kar, N. Bose, B. Dutta, S. Banerjee, N. Mukherjee and S. Mukherjee., 2D SnO_2 nanosheet/PVDF composite based flexible, self-cleaning piezoelectric energy harvester, *Energy Convers. Manage.*, 2019, **184**, 600–608, DOI: 10.1016/j.enconman.2019.01.073.

42 E. Kabir, M. Khatun, L. Nasrin, M. J. Raihan and M. Rahman, Pure β-phase formation in polyvinylidene fluoride (PVDF)-carbon nanotube composites, *J. Phys. D: Appl. Phys.*, 2017, **50**, 163002, DOI: 10.1088/1361-6463/aa5f85.

43 H. Zhou, H. Wang, Z. Liu, H. Yang, C. Yuan and Y. Wang, Facilitated phase transformation of PVDF in its composite with an ionic liquid, *Polymer*, 2021, **220**, 123564, DOI: 10.1016/j.polymer.2021.123564.

44 R. Gregorio and E. M. Ueno, Effect of crystalline phase, orientation and temperature on the dielectric properties of poly(vinylidene fluoride) (PVDF), *J. Mater. Sci.*, 1999, **34**(18), 4489–4500, DOI: 10.1023/A:1004689205706.

45 A. Adaval, C. K. Subash, V. H. Shafeeq, M. Aslam, T. W. Turney, G. P. Simon and A. R. Bhattacharyya, A comprehensive investigation on the influence of processing techniques on the morphology, structure, dielectric and piezoelectric properties of poly(vinylidene fluoride)/Graphene oxide composites, *Polymer*, 2022, **256**, 125239, DOI: 10.1016/j.polymer.2022.125239.

46 P. K. Mahato, A. Seal, S. Garain and S. Sen, Effect of fabrication technique on the crystalline phase and electrical properties of PVDF films, *Mater. Sci.*, 2015, **33**(1), 157–162, DOI: 10.1515/msp-2015-0020.

47 S. Kaur and D. P. Singh, Significantly improved dielectric and energy storage behavior of the surface functionalized $CaCu_3Ti_4O_{12}$ nanoparticles in PVDF-$CaCu_3Ti_4O_{12}$ composites, *J. Alloys Compd.*, 2022, **918**, 165500, DOI: 10.1016/j.jallcom.2022.165500.

48 C. Li, S. Yu, S. Luo, W. Yang, Z. Ge, Z. Huang, R. Sun and C. Wong, Enhancement of dielectric performance up to GHz of the composites with polymer encapsulated hybrid BaTiO 3-Cu as fillers: multiple interfacial polarizations playing a key role, *RSC Adv.*, 2016, **6**, 36450–36458, DOI: 10.1039/C6RA03469A.

49 C. Chang, V. H. Tran, J. Wang, Y. K. Fuh and L. Lin, Direct-Write Piezoelectric Polymeric Nanogenerator with High Energy Conversion Efficiency, *Nano Lett.*, 2010, **10**(2), 726–731, DOI: 10.1021/nl9040719.

50 W. Yang, S. Yu, R. Sun, S. Ke, H. Huang and R. Du, Electrical modulus analysis on the Ni/CCTO/PVDF system near the percolation threshold, *J. Phys. D: Appl. Phys.*, 2011, **44**, 475305, DOI: 10.1088/0022-3727/44/47/475305.

51 S. Shetty, S. Murugesan, S. Salehi, A. Pellert, M. Scheibel, T. Scheibel and S. Anandhan, Evaluation of piezoelectric behavior and biocompatibility of poly(vinylidene fluoride) ultrafine fibers with incorporated talc nanosheets, *J. Appl. Polym. Sci.*, 2022, **139**, e52631, DOI: 10.1002/app.52631.

52 M. Z. Ongun, S. Oguzlar, E. C. Doluel, U. Kartal and M. Yurddaskal, Enhancement of piezoelectric energy-harvesting capacity of electrospun β-PVDF nanogenerators by adding GO and rGO, *J. Mater. Sci.: Mater. Electron.*, 2020, **31**, 1960–1968, DOI: 10.1007/s10854-019-02715-w.

53 Y. Rao, K. M. McEachern and D. P. Arnold, A compact human-powered energy harvesting system, *J. Phys.: Conf. Ser.*, 2013, 12011, DOI: 10.1515/ehs-2013-0023.

54 J. Liu, B. Yang, L. Lu, X. Wang, X. Li, X. Chen and J. Liu, Flexible and lead-free piezoelectric nanogenerator as self-powered sensor based on electrospinning BZT-BCT/P(VDF-TrFE) nanofibers, *Sens. Actuators, A*, 2020, **303**, 111796, DOI: 10.1016/j.sna.2019.111796.